

Fluid-driven fracture propagation in heterogeneous media: Probability distributions of fracture trajectories

David Santillán*

Departamento de Ingeniería Civil: Hidráulica, Energía y Medio Ambiente, Universidad Politécnica de Madrid, Spain

Juan-Carlos Mosquera

Departamento de Mecánica de Medios Continuos y Teoría de Estructuras, Universidad Politécnica de Madrid, Spain

Luis Cueto-Felgueroso

Departamento de Ingeniería Civil: Hidráulica, Energía y Medio Ambiente, Universidad Politécnica de Madrid, Spain

(Received 3 July 2017; revised manuscript received 9 October 2017; published 17 November 2017)

Hydraulic fracture trajectories in rocks and other materials are highly affected by spatial heterogeneity in their mechanical properties. Understanding the complexity and structure of fluid-driven fractures and their deviation from the predictions of homogenized theories is a practical problem in engineering and geoscience. We conduct a Monte Carlo simulation study to characterize the influence of heterogeneous mechanical properties on the trajectories of hydraulic fractures propagating in elastic media. We generate a large number of random fields of mechanical properties and simulate pressure-driven fracture propagation using a phase-field model. We model the mechanical response of the material as that of an elastic isotropic material with heterogeneous Young modulus and Griffith energy release rate, assuming that fractures propagate in the toughness-dominated regime. Our study shows that the variance and the spatial covariance of the mechanical properties are controlling factors in the tortuosity of the fracture paths. We characterize the deviation of fracture paths from the homogenous case statistically, and conclude that the maximum deviation grows linearly with the distance from the injection point. Additionally, fracture path deviations seem to be normally distributed, suggesting that fracture propagation in the toughness-dominated regime may be described as a random walk.

DOI: [10.1103/PhysRevE.96.053002](https://doi.org/10.1103/PhysRevE.96.053002)

I. INTRODUCTION

The hydraulic fracturing process is widely present in geomechanics. A natural example is the fracture generated by the migration of magma through the lithosphere, resulting in thin dikes and sills, which extend over several kilometers [1,2]. Some man-made examples arise from the engineering field, for instance, the geologic sequestration of carbon dioxide [3], the stimulation of geothermal reservoirs to increase heat extraction [4,5], or the enhanced oil and gas extraction from unconventional low-permeability reservoirs [6,7]. The latter two applications have a growing interest which arise from environmental concerns. Heat extraction from geothermal reservoirs has the potential to become a crucial source of renewable carbon-free energy [8]. Unconventional oil and gas are expected to boost energy supply by 2035 [9], and technically recoverable unconventional gas resources worldwide from low-permeability reservoirs are roughly estimated around 8×10^{15} cubic feet [10].

One of the major concerns of the application of hydraulic fracturing technologies is the groundwater contamination. Created fractures may unintentionally connect the reservoir and the surrounding environment, providing hydraulic access between both, and leading to leakage of, fracturing fluid or gas [11,12]. Fracture propagation has a stochastic component, which results into complex trajectories. Experiments have shown that fracture trajectories are highly affected by the *in*

situ stress [13,14], heterogeneity of the reservoir formations [15,16], or the presence of natural fractures [17], among other factors. These effects have also been studied through complex numerical simulations [18–20].

Estimating the uncertainties in fracture propagation through numerical simulations is a challenging task. Monte Carlo simulation method is the simplest and widest-used approach to estimate uncertainty [21]. The biggest disadvantage is that a large number of realizations are required. The influence of the input parameters on the model output can be quantified in the local or global context. The former keeps fixed all the inputs while varying one of them. The latter conducts sensibility analyses through, for instance, stochastic multiscale methods [22,23]. Another approach is the stochastic finite element method, but unfortunately its applications are mostly limited to linear problems [24], although some attempts to extend the method to the nonlinear problem have been performed [25,26]. Some attempts to quantify the uncertainty associated with fracture process due to heterogeneous material properties have been conducted within the Monte Carlo simulation framework [21,27].

The estimate of uncertainty of fluid-driven fracture paths through the Monte Carlo simulation framework requires both a random field generator algorithm of mechanical properties, and a mathematical model of the fracture process. Techniques for generating random fields can be broadly grouped into discrete and continuous models [28]. The former generate random fields of discrete properties, for instance, the number of fractures in fracture networks. On the other hand, continuous models describe properties that vary continuously, for instance,

*david.santillan@upm.es

the Young modulus or the hydraulic conductivity. The most common continuous models are [29] the moving average methods, the discrete Fourier transform (DFT) method, the covariance matrix decomposition, the fast Fourier transform (FFT) method, the turning bands method, and the local average subdivision method.

Fluid-driven fracture propagation in elastic media can be simulated through analytical and numerical models. Analytical solutions are available for simple injection protocols and fracture geometries. Reference [30] provides a review of the state of the art for the penny-shaped fracture propagation. More complex geometries or injection protocols require numerical models.

Numerical models for fluid-driven fracturing can be classified into discrete or continuous approaches. In the discrete approaches, fractures are simulated as discontinuities. Some discrete models are implemented using the finite element method (FEM), where the propagation of the fractures may be simulated by splitting nodes [31], breaking elements [32], enriching the displacement field with new degrees of freedom [33,34], or using cohesive interface elements [35]. Other models are the spring network approach, where fractures grow by splitting nodes and reconnecting springs [36], or the mesh-free methods including the cracking particle method [37,38], the immersed particle method [39], or the discrete element approach [40,41].

Continuous approaches describe both the intact solid and fracture domains as a unique continuum. The geometric simplicity and the topology of the discretization is held during the fracture propagation, which makes these models computationally appealing. Examples of continuous approaches include peridynamics, in which the solid is assumed to be composed of material points that interact with all its neighbors within a nonlocal region called horizon [42–45], or the screen-Poisson method where fractures are regularized through a screened Poisson equation [46].

A novel continuous mathematical approach for fluid-driven fracture propagation in brittle elastic media is the phase-field model. It is based on the Griffith interpretation to model quasistatic brittle fracture propagation [47]. Fractures are treated as a diffuse interface defined by the phase-field variable that interpolates between the broken and unbroken regions. This approach enjoys the following advantages [48]: (i) the approach is fixed mesh; (ii) the formulation is based on energy minimization and, consequently, nucleation, propagation, joining, or branching are automatically computed without any additional handling; and (iii) fracture propagation in heterogeneous media is simulated without any additional modification in the computational framework. Moreover, its capability of simulating fluid-driven fracturing in an elastic medium has been assessed against analytical solutions with encouraging results [49], and compared with laboratory experiments with promising performance [50].

Here, we study the uncertainty of fluid-driven fracture trajectories associated to heterogeneity of rock mechanical properties. We adopt a Monte Carlo simulation framework where random fields of several mechanical properties are generated through a FFT method. We quantify the influence of the mechanical parameters on the fracture path in the local context. Moreover, fracture trajectories are simulated using a

phase-field approach. For simplicity, we restrict our study to a two-dimensional (2D) elastic case study under plain strain conditions, infinitesimal deformations, and isothermal conditions. We assume fractures propagate under the toughness dominated regime with no-fluid lag. The main physical consequence of these assumptions is the restriction of our conclusions to very low permeable rocks where a low-viscous fluid is injected. This situation is quite real since hydraulic fracturing is a technique for enhancing oil and gas production in formations with low permeability. Moreover, fracturing jobs are more efficient when fractures propagate under the toughness-dominated regime since the energy expended in fracturing the rock is much larger than the viscous dissipation [51]. The no-fluid lag assumption is valid when the confining stress is sufficient large [52], although the literature about modeling hydraulic fracturing with fluid-lag is scarce [53,54]. The simulated trajectories allow us to characterize and statistically quantify the influence of several statistical parameters of the random fields on the tortuosity in fracture trajectories. The research question is, then, how rock heterogeneity makes the fracture trajectory deviate from the deterministic path, whether the deviations follows random walks or not, and how far fractures deviate.

The paper is organized as follows. Section II provides the governing equations of the Monte Carlo simulation framework. First, we introduce the random field generator algorithm of mechanical properties of the elastic medium. Afterward, the fluid-driven fracture model based on the phase-field approach is presented. A case study where we apply the methodology is described in Sec. III. The results of the numerical simulations and their analyses are reported in Sec. IV. Finally, some conclusions are drawn in Sec. V.

II. METHODOLOGY

In this section, we begin by describing the geometric representation of the fracture and matrix domains. We then introduce the methodology used to generate correlated synthetic random fields of Young modulus and Griffith energy release rate through a Fourier space method. Finally, we describe the phase-field approach for the simulation of quasistatic, brittle, fluid-driven fracture propagation in elastic solids.

A. Geometry

Consider a domain $\Omega \subset \mathbb{R}^\delta$ with spatial dimension $\delta \in \{2, 3\}$. The problem domain comprises an impermeable elastic subdomain, Ω_E , and a pressurized fracture subdomain, Ω_F ; i.e., $\Omega = \Omega_E \cup \Omega_F$. A slightly compressible Newtonian fluid is injected into the fracture at known pressure. While no mass exchange occurs between subdomains, the fluid pressure exerts a force over the elastic subdomain that induces the propagation on the fracture. The boundary of Ω_i is denoted by $\partial\Omega_i$, where $i = E, F$. The boundary of Ω_E is divided into two subsets, $\partial_D\Omega_E$ and $\partial_N\Omega_E$, where Dirichlet and Neumann boundary conditions are imposed, respectively.

B. Random field generator

We assume that the heterogeneous mechanical properties of real materials can be described, at the macroscopic scale, as a

random yet continuous spatial variation of these quantities. The random field theory [55], through the design of suitable random field generators, is a common tool for modeling this spatial variability. The cornerstone of this approach is the selection of a probability distribution that matches the natural distribution of the property concerned.

Numerous field data analyses and experimental studies have been conducted to characterize the probability distribution of constitutive properties in natural and engineered materials. The hydraulic transmissivity, conductivity, and storage coefficient of aquifers have been found to follow log-normal distributions [56]. Mechanical properties are often found to be log-normally distributed, from the elastic modulus and strength of concrete [57], to the geomechanical parameters of rocks [58] and the elastic modulus of the cytoskeletal network of living cells [59]. Given the ubiquitous presence of log-normal properties in nature, the log-normal distribution has been adopted in many studies to describe material properties in synthetic models. Some examples include the hydraulic properties of soil in probabilistic slope stability analysis [60], infiltration and unsaturated flow [61], flow through porous rocks [62,63] or macrodispersion in aquifers [64]. It has also been adopted to describe the mechanical properties of steel in fatigue and fracture analyses of bridges [65], or the cohesion and friction angle of rocks in the design of rock slopes [66,67].

Here, we consider both the Young modulus, E , and the Griffith energy release rate, G_c , to be isotropic and stationary log-normal fields. We do not consider spatial variations in the Poisson ratio, ν , which is rather taken as a deterministic constant throughout the domain. The assumption of stationarity is appropriate when a single material is modeled, and it implies that all values of a given mechanical property at different points of the solid are drawn from the same distribution with the same statistical parameters.

Given a random field H in a spatial domain D , $\{H(\mathbf{x}); \mathbf{x} \in D \subseteq \mathbb{R}^d\}$, following a log-normal distribution with mean μ_H and standard deviation σ_H , its logarithm, $\ln H$, is normally distributed with mean, $\mu_{\ln H}$, and standard deviation, $\sigma_{\ln H}$, given by:

$$\sigma_{\ln H}^2 = \ln(1 + \sigma_H^2/\mu_H^2), \quad (1)$$

and

$$\mu_{\ln H} = \ln(\mu_H) - \frac{1}{2}\sigma_{\ln H}^2. \quad (2)$$

We assume that values of H at two points in the domain show correlation that decreases with the distance between them. Correlation is modeled through the so-called spatial correlation function. Here we adopt an isotropic Gaussian-type function, $\rho(r)$, which is commonly used to describe geologic materials [68]:

$$\rho(r) = \sigma_{\ln H}^2 \exp(-r/(\sqrt{2}l_c))^2, \quad (3)$$

where r is the spatial distance and l_c is the correlation length. Points separated by distances larger than l_c are weakly correlated and therefore essentially independent. We assume that both fields, E and G_c , have the same correlation function. The field $\ln H$ is expressed as:

$$\ln H(\mathbf{x}) = \mu_{\ln H} + \sigma_{\ln H} Z(\mathbf{x}), \quad (4)$$

where $Z(\mathbf{x})$ follows a standard normal distribution with spatial autocorrelation $\rho(r) = \exp[-r/(\sqrt{2}l_c)]$. We generate random Gaussian fields efficiently through a spectral approach based on the fast Fourier transform (FFT) method [69]. Random fields in the spatial domain, $Z(\mathbf{x})$, are obtained as the inverse Fourier transform of independent random Fourier increments, which are generated on a wave number grid [70].

Regarding the dependence between the $E(\mathbf{x})$ and $G_c(\mathbf{x})$ fields, we assume that at a given location \mathbf{x}_i both log-normal fields depend on each other through only the local variable $Z(\mathbf{x}_i)$ as follows:

$$\ln E(\mathbf{x}_i) = \mu_{\ln E} + \sigma_{\ln E} Z(\mathbf{x}_i), \quad (5)$$

$$\ln G_c(\mathbf{x}_i) = \mu_{\ln G_c} + \sigma_{\ln G_c} Z(\mathbf{x}_i), \quad (6)$$

or, alternatively,

$$\ln E(\mathbf{x}_i) = a \ln G_c(\mathbf{x}_i) + b, \quad (7)$$

where the constants a and b are

$$a = \frac{\sigma_{\ln E}}{\sigma_{\ln G_c}}, \quad (8)$$

$$b = \frac{\mu_{\ln E} \sigma_{\ln G_c} - \mu_{\ln G_c} \sigma_{\ln E}}{\sigma_{\ln G_c}}. \quad (9)$$

The above assumption implies that the correlation coefficient between both variables is one. It is motivated by the fact that in the same material the elastic modulus and the strength are closely related.

C. Rock damage model

We model the propagation of fluid-driven fractures through a quasistatic phase-field formulation. A detailed description of the model formulation can be found in Ref. [49]. Fractures are simulated as diffuse interfaces defined by the phase-field variable, $d \in [0,1]$, which can be interpreted as a damage indicator. We define $d \rightarrow 1$ at the fracture and $d = 0$ at the undamaged regions. In the following formulation, we adopt an anisotropic damage formulation [71], which allows for fracturing in tension only. The anisotropic formulation provides realistic fracture evolution patterns for rocks and other materials with asymmetric response for fracturing under tension and compression. The equilibrium equations for the damage model are given by:

$$-\nabla \cdot \{[g(d) + \kappa]\sigma_0^+ + \sigma_0^-\} - p_f \nabla g(d) - \bar{\mathbf{f}} = \mathbf{0}, \quad \text{in } \Omega, \quad (10)$$

$$\sigma \bar{\mathbf{n}} = \bar{\mathbf{t}}, \quad \text{in } \partial_N \Omega, \quad (11)$$

where σ_0^\pm refers to Cauchy tensile or compressive stresses in the undamaged solid, $g(d)$ is a degradation function, κ is a small positive parameter, p_f is the pressure of the fluid inside the fracture, $\bar{\mathbf{f}}$ is the body force vector per unit volume, $\bar{\mathbf{t}}$ is the vector of applied traction surface forces, and $\bar{\mathbf{n}}$ is the outward normal unit vector. The small positive parameter $\kappa \approx 0$ prevents numerical singularities and is chosen as small as possible such that the algebraic conditioning number of the numerical method guarantees well-posedness for partly broken systems [72].

The tensile or compressive stress σ_0^\pm is given by:

$$\sigma_0^\pm(\mathbf{u}) = \sum_{a=1}^{\delta} \left[\lambda \left\langle \sum_{i=1}^{\delta} \varepsilon_i \right\rangle_{\pm} + 2\mu \langle \varepsilon_a \rangle_{\pm} \right] \mathbf{n}_a \otimes \mathbf{n}_a, \quad (12)$$

where $\langle x \rangle_{\pm} = (x \pm |x|)/2$, λ and μ are the Lamé constants, δ is the number of space dimensions, ε_a is the a th principal strain, and \mathbf{n}_a is the principal strain direction associated to the principal strain ε_a . The eigenvalue bases $\mathbf{n}_a \otimes \mathbf{n}_a$ are computed in terms of the principal strains ε_i and the strain tensor ε as follows [73]:

$$\mathbf{n}_a \otimes \mathbf{n}_a = \frac{1}{\prod_{b \neq a}^{\delta} (\varepsilon_a - \varepsilon_b)} \prod_{b \neq a}^{\delta} (\varepsilon - \varepsilon_b \mathbf{1}). \quad (13)$$

We employ a quadratic degradation function $g(d) = (1 - d)^2$ [74]. While other degradation functions have been proposed in the literature, the impact of its particular functional form diminishes after the fracture has formed [75], and Γ convergence has so far only been proved for the quadratic polynomial [76].

The strong form of the phase-field problem reads:

$$\frac{g_c}{\ell} (d - \ell^2 \nabla^2 d) = 2(1 - d)H^+, \quad \text{in } \Omega, \quad (14)$$

$$\nabla d \cdot \mathbf{n} = 0, \quad \text{in } \partial_N \Omega, \quad (15)$$

where ℓ is the length scale parameter, and H^+ is the maximum local history field. The characteristic length ℓ controls the band width across which the regularization of the fracture surface takes place. Phenomena with characteristic length scales smaller than ℓ cannot be captured by our model, e.g., the observed self-affine scaling of fracture roughness [77]. Numerically, ℓ has a slight influence over the critical load that triggers unstable fracture propagation—the load decreases as ℓ increases [50,74]. The memory term H^+ is the maximum historic energy generated by tensile strain, and is given by:

$$H^+(\mathbf{u}, p_f, t) = \max_{s \in [0, t]} [\psi_0^{e+}(\varepsilon) + p_f \nabla \cdot \mathbf{u} + \mathbf{u} \cdot \nabla p_f] \quad (16)$$

where \mathbf{u} is the displacement field, t is time, and ψ_0^{e+} is the positive undamaged elastic energy density. More generally, $\psi_0^{e\pm}$ splits the total energy among tension and compression as follows:

$$\psi_0^{e\pm}(\varepsilon) = \frac{\lambda}{2} \left(\left\langle \sum_{i=1}^{\delta} \varepsilon_i \right\rangle_{\pm} \right)^2 + \mu \sum_{i=1}^{\delta} \langle \varepsilon_i \rangle_{\pm}^2, \quad (17)$$

and fulfills $\psi_0^e(\varepsilon) = \psi_0^{e+}(\varepsilon) + \psi_0^{e-}(\varepsilon)$. Irreversibility is enforced in the model through H^+ , which ensures that damaged regions do not heal, even when stress disappears [71].

We consider that fractures propagate under the toughness-dominated regime, i.e., the energy expended in fracturing the rock is much larger than the viscous dissipation due to the movement of the fluid inside the fracture [78]. We further assume that the fluid viscosity is negligible, and as a result fluid pressure inside the fracture is uniform and equal to the prescribed boundary pressure. Consequently, since the pressure inside the fracture is uniform and its value is known at the injection point, there is no need to solve the flow equation along the fracture to update p_f . Since the fracture domain is

modeled as a field, the fracture path has to be inferred from the phase field. In our 2D setting, the trajectory is the line where the gradient of the phase field is zero and the phase field is above a threshold d_f (here we adopt $d_f = 0.9$ [49]).

The coupled problem, i.e., the equilibrium equation (10) together with the damage model (14), is implemented using the finite element software COMSOL MULTIPHYSICS [79]. The integration in time is fully implicit and adaptive, and it is based on backward differentiation formulas [80].

III. CASE STUDY

We simulate the propagation of a single fracture under the toughness-dominated regime in an elastic solid whose Young modulus and Griffith critical energy release rate spatially vary following stationary isotropic log-normal fields (Fig. 1). Since our main purpose is to investigate the effect of the spatial variability of E and G_c , we consider ν and the boundary conditions to be deterministic. The domain is a square of side 60 m, and an initial horizontal fracture of length 0.2 m is located at the center of the left side, Fig. 1(a). We inject fluid at prescribed pressure through a point located at (0,0) in the left side of the fracture. The boundary conditions are

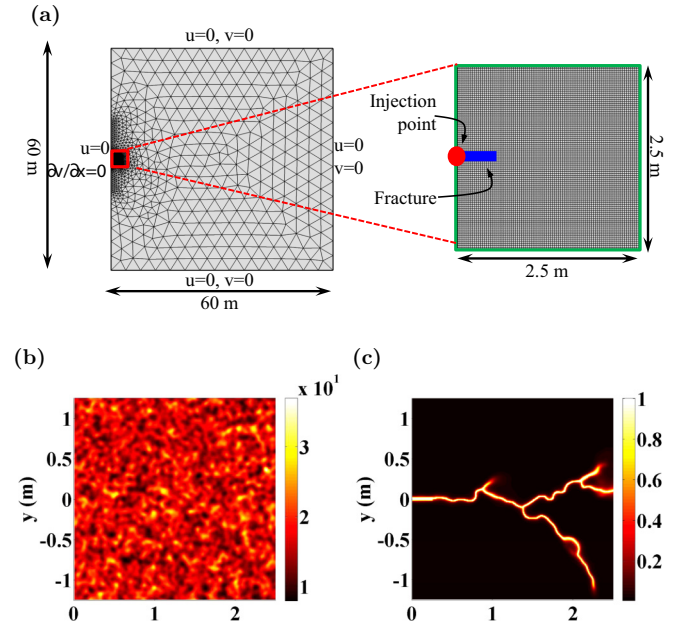


FIG. 1. Schematic description of the case study: problem geometry, computational mesh, and illustration of the relevant fields. (a) We simulate fluid injection at prescribed pressure, and study the propagation of an initially horizontal fracture of length 0.2 m. The outer domain boundaries are fixed except at the left side, where we impose symmetric displacements. The computational mesh is structured in the inner domain, with four-noded quadrilateral elements, and unstructured in the outer domain with three-noded triangular elements. Maximum mesh sizes in the inner and outer domains are, respectively, 8 mm and 4 m. (b) A realization of log-normal Young modulus with Gaussian spatial correlation function. The mean is μ_E is 17 GPa, σ_E is 3.4 GPa, μ_{g_c} is 100 Pa m, σ_{g_c} is 20 Pa m, and the correlation length is l_c is 0.10 m. (c) Using the previous realization, we simulate the fracture propagation. Here we show a map of the phase-field variable at the end of the simulation.

zero displacements, except at the left side where symmetry boundary conditions are imposed. We assume plane strain conditions.

We minimize boundary effects by studying the fracture propagation inside an inner square of side 2.5 m [red square of Fig. 1(a)] where we use a highly refined mesh. The outer domain is discretized as an unstructured mesh with linear triangular elements of maximum size 4 m, while the inner domain comprises four-noded quadrilateral elements whose size is selected through a convergence study.

Given one realization of E and G_c , we simulate the propagation of the initial seed fracture with mesh sizes ranging from 2×10^{-2} m to 4×10^{-3} m, Fig. 2(a). We then compute the root-mean-square deviation, S_r , of the simulated fracture paths with respect to the result provided by the simulation with the smallest mesh size, Fig. 2(b). The damaged area provided by the phase-field variable has the same dimension as the domain, but it shrinks and converges to the fracture path as the mesh size is smaller, Figs. 2(c)–2(d). The values of S_r for the considered sizes suggest that a good choice is $\delta_x = \delta_y = 8$ mm, which provides results that are very similar to the simulations with the smallest size. As a reference, the mesh shown in Fig. 2(a) is composed of 15161 triangular elements and 97969 square elements.

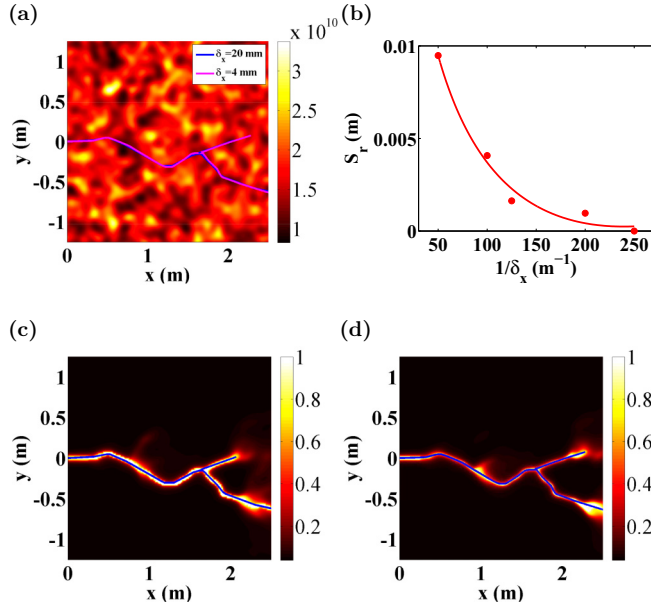


FIG. 2. Mesh convergence study of the fracture trajectories. (a) We plot one realization of 2D log-normal Young modulus with a Gaussian correlation function. μ_E is 17 GPa, σ_E is 3.4 GPa, μ_{G_c} is 100 Pa m, σ_{G_c} is 20 Pa m, and l_c is 0.10 m. The fracture paths computed with inner mesh sizes of 20 and 4 mm are depicted in blue and magenta respectively. (b) Here we depict the value of S_r of the fracture path for every simulation, taking as reference solution the simulation with the smallest size. The solution converges to the reference case as the mesh size is smaller. We depict the phase-field variable calculated with an inner mesh size of 20 and 4 mm and the fracture paths in blue in (c) and (d), respectively. As the mesh size is smaller, the 2D damaged area shrinks and converges to the fracture path.

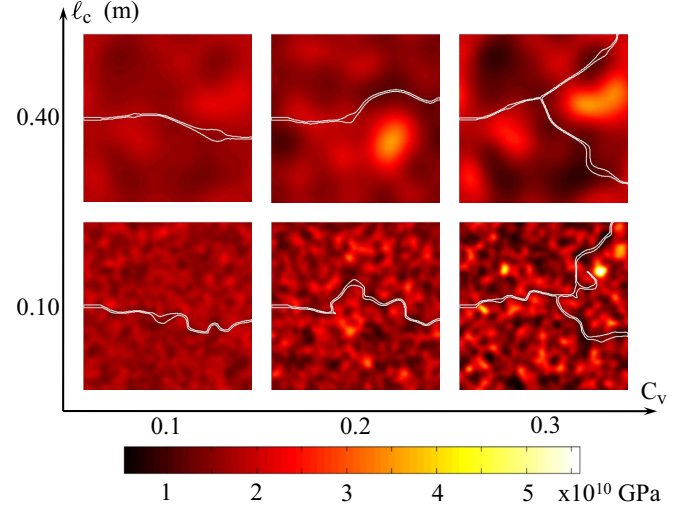


FIG. 3. Schematic description of the influence of C_v and l_c . We plot one realization of the Young modulus for some values of C_v and l_c . In the same panels we also plot in white the fracture paths. It can be appreciated how the trajectories become more tortuous as either the variability of the Young modulus or the correlation length increase. The fracture propagates following the weakest regions, which in our simulations also have the lowest values of the Young modulus.

In the simulations analyzed in the next section, the mechanical properties of the elastic solid are: mean Young modulus $\mu_E = 17$ GPa, mean Griffith critical energy release rate $\mu_{G_c} = 100$ Pa m, Poisson ratio $\nu = 0.2$, and length scale parameter $\ell = 4 \times 10^{-2}$ m. We depict one realization of the Young modulus field in Fig. 1(b), where σ_E is 3.4 GPa, σ_{G_c} is 20 Pa m, and the correlation length is 0.10 m. The injection pressure varies from 1 MPa at time zero to 4 MPa at time 7.2×10^3 s. We stop the simulation when the fracture reaches any of the sides of the inner domain. The key result of the simulation is the phase-field variable, which provides the fracture path. As an example of a typical fracture evolution, we show the phase-field variable at the end of a simulation in Fig. 1(c), which corresponds to the realization of Young modulus field shown in Fig. 1(b).

IV. NUMERICAL RESULTS AND DISCUSSION

We study the influence of the statistical properties of the heterogeneous fields E and G_c on the fracture trajectories. These trajectories can be understood as perturbations of the homogeneous case—with uniform mean values of E and G_c —for which fractures propagate along a straight path. Spatially variable mechanical properties make fractures deviate from the straight trajectory and even branch, corresponding to random propagation. We illustrate several random fracture trajectories in Fig. 3, where we plot one realization of the Young modulus for some values of the coefficient of variation, $C_v = \sigma/\mu$, and the correlation length, l_c . In the same panels we also plot the simulated fracture paths in white. It can be appreciated how the variability of the fields increases with C_v , how the size of the regions with a similar magnitude of the field becomes larger with l_c , and how the trajectories become more tortuous as either C_v increases or l_c decreases. The strongest regions

TABLE I. Simulated data sets. The mean value of the Young modulus, μ_E , is taken 17 GPa, and the Griffith energy release rate, μ_{gc} , 100 Pa m.

Set	C_v	l_c (m)
1	0.1	0.10
2	0.2	0.10
3	0.3	0.10
4	0.2	0.05
5	0.2	0.15
6	0.2	0.20
7	0.2	0.40

are those with the highest value of E , and are coincident with the largest G_c . The fractures propagate following the weakest regions, depicted in dark colors, and try to avoid the strongest ones. This result is in agreement with some experiments conducted in concrete with different aggregate strengths [81].

We analyze the effects of C_v and l_c on the fracture path in the local context, i.e., we fix one of the parameters while varying the other one. We consider seven data sets of statistical parameters, listed in Table I, where sets correspond to three values of $C_v = \{0.1, 0.2, 0.3\}$ for constant $l_c = 0.10$ m, and five values of $l_c = \{0.05, 0.10, 0.15, 0.20, 0.40\}$ m for constant $C_v = 0.2$. The mean value of the Young modulus, μ_E , is taken 17 GPa, and the Griffith energy release rate, μ_{gc} , 100 Pa m. For each value set of the statistical parameters, we simulate fracture propagation on 1000 realizations of the random mechanical property fields

We include Fig. 4(a) for illustrative purposes, where we depict the contour plot of one realization of the Young modulus field of the inner domain with $C_v = 0.2$ and $l_c = 0.10$ m. We also plot the fracture path in white. For each parameter combination, we show the 1000 fracture trajectories Fig. 4(b) (gray). In the same figure we also indicate the trajectory shown in Fig. 4(a) with a black solid line. With this raw data, we analyze the fracture path uncertainty in terms of C_v , and l_c . The mesh size is small enough to capture the spatial variability of the random fields imposed by l_c . In the following sections we describe our analyses and discuss our findings.

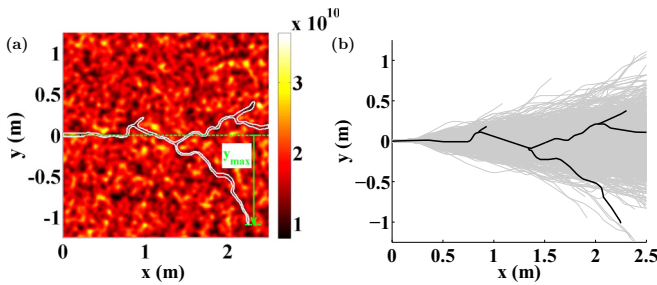


FIG. 4. Monte Carlo simulation framework. (a) We plot one realization of 2D log-normal Young modulus with a Gaussian correlation function. μ_E is 17 GPa, σ_E is 3.4 GPa, μ_{gc} is 100 Pa m, σ_{gc} is 20 Pa m, and l_c is 0.10 m. The fracture path is shown in white. (b) Here we depict in gray the fracture paths of 1000 realizations of random E fields, and in black the fracture path corresponding to the realization shown in (a).

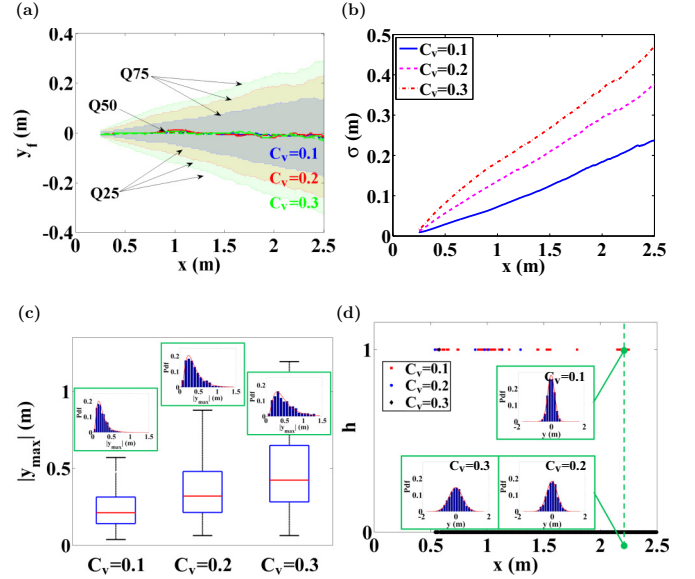


FIG. 5. Influence of C_v on the hydraulic fracture paths. (a) We plot the quartiles of the deviation, y , of the fracture path from the deterministic trajectory for three values of C_v . The initial seed fracture extends between points (0,0) and (0.2,0). A constant value of x , larger values of C_v implies a larger interquartile distance of y , i.e., larger uncertainty. Also, for a given C_v , the interquartile distance increases linearly with the distance to the injection point. (b) Evolution of the standard deviation of y , σ , along the coordinate x , for three values of C_v . σ increases with the heterogeneity of the medium, and linearly with the distance to the injection point. (c) Box plot of the maximum deviation y_{\max} of each fracture path for the three considered values of C_v . In the upper part of the box plots we show the histograms of y_{\max} in blue and the fitted log-normal distributions in solid red line. The Kolmogorov-Smirnov test indicates that y_{\max} can be modeled as log-normal in all cases. (d) We fit normal distributions to the deviation y at each x position, and plot the result of the Kolmogorov-Smirnov test to check whether the simulated data follow normal distributions—null hypothesis. We also depict three histograms in blue and the fitted normal distributions in solid red line.

A. Influence of the coefficient of variation

We run 1000 realizations for each considered value of C_v , with the correlation being $l_c = 0.10$ m. We study three values of $C_v = \{0.1, 0.2, 0.3\}$, resulting in three data sets of statistical parameters of the mechanical properties. We simulate the fracture propagation for each realization, a total of 3000 paths. We will refer to y as the vertical distance between the simulated fracture propagation and the deterministic one at a given x position. In other words, the deviation of the fracture path from the straight, horizontal one. Since the computational mesh in the propagation area is composed of four-noded structured quadrilateral elements, there will be at least $(2.5 - 0.2)/0.008 = 288$ values of y for a single fracture path, where 2.5 m refers to the horizontal length of the propagation domain, 0.2 m is the length of the initial fracture, and 0.008 m is the mesh size.

Using all the simulated fracture paths for a given data set of statistical parameters, we compute the quartiles of the variable y at each x position of our computational mesh. We plot the quartiles for each value of C_v in Fig. 5(a), where the injection

TABLE II. Root-mean-square deviation, S_r , between the probability of the data sets 1–7 to the selected distributions: log-normal, Weibull, Gumbel, and gamma. The log-normal distribution provides the best fit followed by the gamma distribution.

Set	Log-normal	Weibull	Gumbel	Gamma
1	1.35×10^{-2}	3.24×10^{-2}	1.12×10^{-1}	1.99×10^{-2}
2	1.06×10^{-2}	3.44×10^{-2}	1.04×10^{-1}	2.18×10^{-2}
3	1.68×10^{-2}	2.86×10^{-2}	8.80×10^{-2}	1.93×10^{-2}
4	1.12×10^{-2}	3.82×10^{-2}	1.22×10^{-1}	2.29×10^{-2}
5	9.93×10^{-3}	3.31×10^{-2}	1.01×10^{-1}	2.99×10^{-2}
6	1.76×10^{-2}	3.83×10^{-2}	1.02×10^{-1}	2.99×10^{-2}
7	1.60×10^{-2}	2.51×10^{-2}	1.01×10^{-1}	1.65×10^{-2}

point is located at (0,0) and the initial fracture extends from that point to (0.2,0). The spatial variability, characterized by C_v , of the mechanical properties has a direct effect on the uncertainty of the fracture paths. For a fixed x position, larger values of C_v imply larger interquartile distance of y , or in other words larger uncertainty. Moreover, for a given value of C_v , the interquartile distance linearly increases with the distance to the injection point. The second quartile (median) is roughly zero in all x positions, and the first and third quartiles are symmetrical with relation to the second one. These results indicate that fractures propagate with the same probability in the positive or negative parts of the y axis, and that the mean behavior corresponds to the deterministic one.

The standard deviation of y , σ , at a given x position increases with C_v [Fig. 5(b)], which is also reflected by the evolution of the second and third quartiles with the x coordinate [Fig. 5(a)]. Moreover, for a given value of C_v , the growth of the variance with the x coordinate is linear. The mean of the deviation, not shown in the figure, is zero in all vertical sections.

We determine the maximum absolute value of the deviation, y_{\max} , of each fracture path. We depict the box plots of y_{\max} for the three considered values of C_v in Fig. 5(c). The spatial variability has also a direct influence on the extremal values of y : the median, the inter quartile range, and the whisker length increase with C_v . The evolution of the quartiles is rather linear with C_v , in the sense that the variability of y_{\max} increases with C_v . The upper part of the boxes is bigger than the lower one, which indicates that the probability distributions of y_{\max} are asymmetric.

We fit log-normal, Weibull, Gumbell, and gamma probability distribution functions (PDFs) to the three data sets of y_{\max} . We assess the adjustment through the root-mean-square deviation, S_r , between the probability of the data to the selected distribution, see Table II. The results indicate that the log-normal PDF provides the best fit to the three data sets.

We plot the histograms of y_{\max} in the insets of Fig. 5(c) and the fitted log-normal PDFs to the data in red solid lines. We perform a Kolmogorov-Smirnov test to check whether the simulated data come from log-normal distributions (null hypothesis). The test indicates that the null hypotheses are not rejected at the 5% of significance level in any set. The histograms also show that the mean and the variance of y_{\max} increase with C_v .

We analyze the probability distribution of the deviation at each x position. We fit normal distributions to the three data sets at each vertical cross section, and we perform the Kolmogorov-Smirnov test to check whether simulated data follow normal distributions (null hypothesis). The results of the test [Fig. 5(d)] show that in most cases the null hypotheses cannot be rejected at the 5% of significance level. Moreover, the number of rejected cases decrease as the value of C_v increases. Nevertheless, the rejected cases qualitatively may follow normal distributions. We show this by plotting in blue the histograms of y at the section $x = 2.25$ m for the three considered values of C_v , and in solid red the fitted normal distributions. The test rejects the set with $C_v = 0.1$, although these data qualitatively seem to be normally distributed.

We have found that the deviation of the fracture path from the deterministic trajectory increases with the heterogeneity of the medium. Moreover, at every position of the deterministic fracture, the position of the random trajectories follows a normal distribution whose mean is the deterministic path and the standard deviation increases with the distance to the origin of the fracture. Finally, we have found that this standard deviation linearly increases with the distance, which suggests that fracture trajectories can be described through random walks.

B. Influence of the correlation length

We investigate the uncertainty of the fracture propagation occasioned by the correlation length, l_c , in five data sets of statistical parameters with $l_c = \{0.05, 0.10, 0.15, 0.20, 0.40\}$ m whereas C_v is constant and equals to 0.2. We run 1000 realizations for each data set. We plot the quartiles of y at each x position of the computational mesh for three smallest values of l_c in Fig. 6(a). The influence of the correlation length on fracture trajectories is qualitatively similar to that of C_v : for a fixed position, higher values of l_c imply larger interquartile distance, or in other words, larger uncertainty in the fracture path. As in the previous analysis, the interquartile distance linearly increases with the distance to the injection point. In the same manner, the second quartile (median) is approximately zero in all sections, and the first and third quartiles are also symmetric with respect to the median.

We also compute the quartiles for larger values of l_c , 0.20, and 0.40 m, not shown in Fig. 6(a), but their values are quite similar to those of $l_c = 0.15$ m. We attribute this behavior to the ratio between l_c and the size of the propagation domain. The correlation length is a way to consider the size of the inclusions in the rock (rigid or soft), and the coefficient of variation accounts for the variability in the magnitude of the mechanical properties between the soft and rigid inclusions. As a result, the size of the domain must contain a number of inclusions, enough to properly capture the variability. This number can be estimated as the ratio between the area of the domain and the mean area of one inclusion, considered these ones as circles with radius $\sqrt{2}l_c$ according to Eq. (3). In our square domain of side 2.5 m and $l_c = \{0.05, 0.10, 0.15, 0.20, 0.40\}$ m, the estimated number of inclusions is, respectively, {398, 99, 44, 25, 6}. For values of l_c larger than 0.15 m, the domain does not seem to be big enough to capture the spatial variability of the mechanical properties,

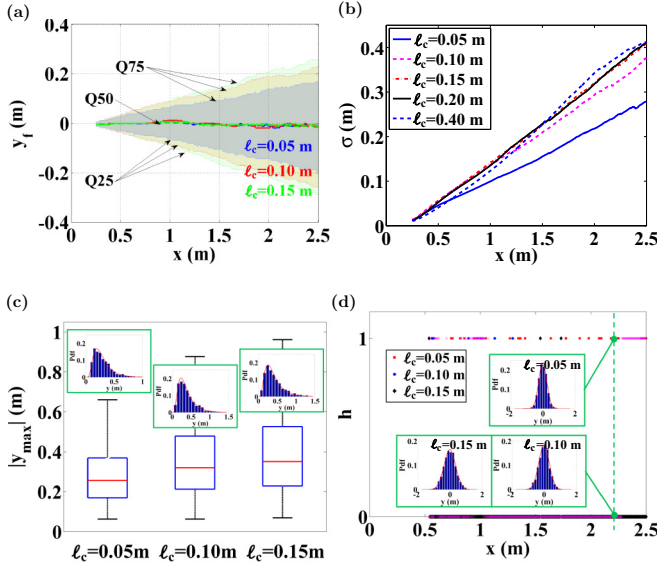


FIG. 6. Influence of l_c on the hydraulic fracture path. (a) Quartiles of the deviation y of fracture paths from the deterministic trajectory for three values of the correlation length, l_c . For a constant value of x , larger values of l_c lead to larger interquartile distance of y , i.e., more uncertainty. Also, for a given l_c , the interquartile distance increases linearly with distance to the injection point. (b) Evolution of the standard deviation of y (σ) with the coordinate x for five values of l_c . For a given x , σ increases with l_c up to $l_c = 0.15$ m, and then σ remains constant for larger values. Also, σ increases with the distance to the injection point, suggesting that fractures deviate further from the straight path as either l_c or the distance to the injection point increase. (c) Box plot of the maximum deviation y_{\max} of each fracture path for the three considered values of l_c . In the upper insets we show the histograms of y_{\max} in blue and the fitted log-normal distributions in solid red line. The Kolmogorov-Smirnov test indicates that y_{\max} can be modeled with log-normal distributions in all cases. (d) Here we plot the result of the Kolmogorov-Smirnov test to check whether simulated deviations y at each x position follow normal distributions (null hypothesis). We also show three histograms in blue and the fitted normal distributions in solid red line.

since the effect of l_c over the deviation of the fractures does not increase. For even larger values of l_c , the domain could become part of just one inclusion and no variability would be captured, i.e., the problem would become deterministic.

The standard deviation of y at a given section increases with l_c [Fig. 6(b)]. Moreover, for a given value of l_c the standard deviation linearly increases with the distance to the injection point. The mean of the deviation, not shown in the figure, is zero at all vertical sections. We also plot the evolution of σ for $l_c = 0.20$ m and 0.40 m, whose aspect is essentially identical to the set with $l_c = 0.15$ m.

We compute y_{\max} of each fracture path and depict the box plots of y_{\max} for the three values of l_c in Fig. 6(c). The median, the interquartile range, and the whisker length increase with l_c , but the rate of the growth decreases for the largest values of l_c . The probability distributions of y_{\max} are asymmetric, and the asymmetry seems to increase with l_c . We fit log-normal, Weibull, Gumbell, and gamma PDFs to the three data sets of y_{\max} and assess the adjustments through the root-mean-square deviation, Table II. The results indicate that

the log-normal PDF provides the best fit to the three data sets. We plot the histograms of y_{\max} in the insets of Fig. 6(c) and the fitted log-normal PDFs to the data in solid red lines. The Kolmogorov-Smirnov test indicates that the null hypotheses (data follow log-normal distributions) are not rejected at the 5% of significance level in any set.

We study the probability distribution of y at each x position. We fit normal distributions to the three data sets at each vertical cross section. The results of the Kolmogorov-Smirnov test [Fig. 6(d)] show that in most cases the null hypothesis (data follow normal distributions) cannot be rejected at the 5% of significance level. As in the previous analysis, the number of rejected cases decrease as the value of l_c rises. Nevertheless, the rejected cases qualitatively may follow normal distributions: we plot in blue the histograms of y at the section $x = 2.25$ m for the three values of l_c , and in solid red the adjusted normal distribution. The test rejects the set of $l_d = 0.05$ m, although apparently follows a normal distribution.

Our main finding is that the correlation length has a similar effect as the heterogeneity of the medium. However, its impact increases with its magnitude up to a value from which it remains constant. We have attributed this effect to the ratio between l_c and the size of the domain, for large values of l_c the domain is not big enough to capture the variability.

V. CONCLUSIONS

A fluid-driven fracture propagating in an homogeneous and isotropic impermeable elastic medium follows a straight trajectory. In contrast, real materials have heterogeneous mechanical properties, which induce deviations of the fracture trajectories. We have analyzed the influence of the spatial variability of mechanical properties on the complexity and spatial structure of the trajectories of fluid-driven fractures. In particular, we characterized the deviations of fracture trajectories from the straight, deterministic path. For this purpose, we have generated log-normal isotropic random fields of the Young modulus and the Griffith energy release rate. These random correlated fields are statically defined by the coefficient of variation, C_v , the ratio between the standard deviation and the mean of the field, and the correlation length, l_c , a characteristic length, which defines the spatial correlation of the fields.

To focus on the crack growth process, the geometry of our case study is a square domain of side 2.5 m, where an initial horizontal fracture of 0.2 m length is located at the center of the left side. To avoid boundary effects, this refined inner domain is embedded inside a larger square domain of 60 m. We simulate the pressure-driven propagation of the initial fracture inside the inner domain by conducting numerical simulations based on the phase-field approach under plane strain conditions. Based on these simulations, we studied the deviation of the trajectory of each fracture, $y(x)$, from the deterministic path at several points along the trajectory.

We considered three values of the coefficient of variation with constant l_c , running a thousand realizations of the random mechanical property fields for each value of C_v , and simulated the fracture propagation for each realization. For a fixed position located along the horizontal deterministic fracture path, x , the mean and median of y at that point are equal to

the deterministic value, and the first and third quartiles are symmetrical in relation to the median. However, the standard deviation of y at a given position increases with C_v , and for a given C_v it increases with the distance to the initial fracture. We have also analyzed the probability distribution of y at several positions located in the deterministic fracture path, and we have found that in most of them y can be well represented by normal distributions. We have also found that the absolute maximum value of y of each fracture trajectory follows log-normal distributions whose mean and standard deviation increase with C_v .

We have conducted several analyses to estimate the influence of the correlation length on the fracture trajectories. We have considered five values of l_c , with constant C_v , and run 1000 realizations for each value. We have found that the smallest values of l_c have a similar effect as C_v , i.e., the variability of the fracture trajectories increases with l_c . However, the largest values of l_c have resulted into paths with similar variability. We have attributed this behavior to the ratio between the size of the domain and l_c . Since the domain has constant size, it is unable to properly capture the spatial variability of the mechanical properties for the largest values of l_c . Moreover, for values of l_c comparable to the size of the domain, the fields can even become deterministic.

Our research shows that heterogeneity in the mechanical properties of fracturing materials significantly influences the complexity of fluid-driven fracture trajectories. Not surpris-

ingly, the deviation from the deterministic paths predicted by homogeneous media theories increases with the variability of mechanical properties. This is important in practice for the application of hydraulic fracturing to the stimulation of geothermal reservoirs or the recovery of oil and gas from unconventional reservoirs. In the latter, one of the major concerns is the potential for groundwater contamination due to the unintentional hydraulic connection of the target reservoir with surrounding freshwater bodies [11,12]. These hydraulic connections may arise from stimulated hydraulic fractures that deviate significantly from their expected fracture paths due to heterogeneity. Our research can be the starting point for further developments of statistical procedures to estimate the likelihood that a fracture reaches an aquifer during the hydraulic fracturing processes, among other applications. Moreover, the effect of anisotropy in the random mechanical properties or in the initial stress field are also important open questions.

ACKNOWLEDGMENTS

This research was supported by the Spanish Ministry of Economy and Competitiveness under Grant No. CTM2014-54312-P. L.C.-F. also gratefully acknowledges funding from the Spanish Ministry of Economy and Competitiveness (Grant No. RyC-2012-11704).

-
- [1] A. Rubin, *Annu. Rev. Earth Planet. Sci.* **23**, 287 (1995).
 - [2] D. Spence and D. Turcotte, *J. Geophys. Res.-Solid Earth* **90**, 575 (1985).
 - [3] F. Cappa and J. Rutqvist, *Int. J. Greenh. Gas Control* **5**, 336 (2011).
 - [4] K. F. Evans, H. Moriya, H. Niitsuma, R. H. Jones, W. S. Phillips, A. Genter, J. Sausse, R. Jung, and R. Baria, *Geophys. J. Int.* **160**, 388 (2005).
 - [5] A. Ghassemi, *Geotech. Geol. Eng.* **30**, 647 (2012).
 - [6] T. Patzek, F. Male, and M. Marder, *Proc. Natl. Acad. Sci. USA* **110**, 19731 (2013).
 - [7] L. Cueto-Felgueroso and R. Juanes, *Proc. Natl. Acad. Sci. USA* **110**, 19660 (2013).
 - [8] R. Bertani, *Geothermics* **41**, 1 (2012).
 - [9] BP Global, *BP Energy Outlook 2035* (BP Global, London, 2015).
 - [10] V. Kuuskraa, S. Stevens, and K. Moodhe, *Technically Recoverable Shale Oil and Shale Gas Resources: An Assessment of 137 Shale Formations in 41 Countries Outside the United States* (US Energy Information Administration, Washington, DC, 2013).
 - [11] S. Osborn, A. Vengosh, N. Warner, and R. Jackson, *Proc. Natl. Acad. Sci. USA* **108**, 8172 (2011).
 - [12] R. Vidic, S. Brantley, J. Vandenbossche, D. Yoxtheimer, and J. Abad, *Science* **340**, 1235009 (2013).
 - [13] J. Zhou, M. Chen, Y. Jin, and G. Zhang, *Int. J. Rock Mech. Min. Sci.* **45**, 1143 (2008).
 - [14] Z. Yushi, Z. Shicheng, Z. Tong, Z. Xiang, and G. Tiankui, *Rock Mech. Rock Eng.* **49**, 33 (2016).
 - [15] P. Liu, Y. Ju, P. Ranjith, Z. Zheng, and J. Chen, *J. Nat. Gas Sci. Eng.* **35**, 541 (2016).
 - [16] X. Ma, Y. Zou, N. Li, M. Chen, Y. Zhang, and Z. Liu, *J. Struct. Geol.* **97**, 37 (2017).
 - [17] F. Zhang, E. Dontsov, and M. Mack, *Int. J. Numer. Anal. Methods* **41**, 1430 (2017).
 - [18] L. Li, Q. Meng, S. Wang, G. Li, and C. Tang, *Acta Geotech.* **8**, 597 (2013).
 - [19] N. Nagel, M. Sanchez-Nagel, F. Zhang, X. Garcia, and B. Lee, *Rock Mech. Rock Eng.* **46**, 581 (2013).
 - [20] Z. Yushi, M. Xinfang, Z. Shicheng, Z. Tong, and L. Han, *Rock Mech. Rock Eng.* **49**, 3597 (2016).
 - [21] Z. Yang, X. Su, J. Chen, and G. Liu, *Int. J. Solids Struct.* **46**, 3222 (2009).
 - [22] N. Vu-Bac, R. Rafiee, X. Zhuang, T. Lahmer, and T. Rabczuk, *Compos. Pt. B-Eng.* **68**, 446 (2015).
 - [23] N. Vu-Bac, T. Lahmer, X. Zhuang, T. Nguyen-Thoi, and T. Rabczuk, *Adv. Eng. Softw.* **100**, 19 (2016).
 - [24] G. Stefanou, *Comput. Meth. Appl. Mech. Eng.* **198**, 1031 (2009).
 - [25] J. Baroth, L. Bodé, P. Bressolette, and M. Fogli, *Comput. Meth. Appl. Mech. Eng.* **195**, 6479 (2006).
 - [26] J. Baroth, P. Bressolette, C. Chauvière, and M. Fogli, *Comput. Meth. Appl. Mech. Eng.* **196**, 4419 (2007).
 - [27] Z. Yang and X. Xu, *Comput. Meth. Appl. Mech. Eng.* **197**, 4027 (2008).
 - [28] H. Haldorsen and E. Damsleth, *J. Pet. Technol.* **42**, 404 (1990).

- [29] G. Fenton and D. Griffiths, in *Probabilistic Methods in Geotechnical Engineering* (Springer, Berlin, 2007), pp. 201–223.
- [30] E. Detournay, *Annu. Rev. Fluid Mech.* **48**, 311 (2016).
- [31] M. Wangen, *J. Pet. Sci. Eng.* **77**, 274 (2011).
- [32] P. Fu, S. M. Johnson, and C. R. Carrigan, *Int. J. Numer. Anal. Methods Geomech.* **37**, 2278 (2013).
- [33] N. Moës, J. Dolbow, and T. Belytschko, *Int. J. Numer. Methods Eng.* **46**, 131 (1999).
- [34] J. Oliver, A. Huespe, and P. Sanchez, *Comput. Meth. Appl. Mech. Eng.* **195**, 4732 (2006).
- [35] V. P. Nguyen, H. Lian, T. Rabczuk, and S. Bordas, *Eng. Geol.* **225**, 68 (2017).
- [36] A. Hafver, E. Jettestuen, J. Feder, P. Meakin, and A. Malthesørensen, *Physica A* **416**, 61 (2014).
- [37] T. Rabczuk and T. Belytschko, *Int. J. Numer. Meth. Eng.* **61**, 2316 (2004).
- [38] T. Rabczuk and T. Belytschko, *Comput. Methods Appl. Mech. Eng.* **196**, 2777 (2007).
- [39] T. Rabczuk, R. Gracie, J. H. Song, and T. Belytschko, *Int. J. Numer. Meth. Engng.* **81**, 48 (2010).
- [40] Ø. Johnsen, R. Toussaint, K. J. Måløy, and E. G. Flekkøy, *Phys. Rev. E* **74**, 011301 (2006).
- [41] I. Ghani, D. Koehn, R. Toussaint, and C. W. Passchier, *Pure Appl. Geophys.* **170**, 1685 (2013).
- [42] H. Ouchi, A. Katiyar, J. York, J. T. Foster, and M. M. Sharma, *Comput. Mech.* **55**, 561 (2015).
- [43] H. Ren, X. Zhuang, Y. Cai, and T. Rabczuk, *Int. J. Numer. Meth. Eng.* **108**, 1451 (2016).
- [44] T. Rabczuk and H. Ren, *Eng. Geol.* **225**, 42 (2017).
- [45] S. Oterkus, E. Madenci, and E. Oterkus, *Eng. Geol.* **225**, 19 (2017).
- [46] P. Areias, M. Msekhi, and T. Rabczuk, *Eng. Fract. Mech.* **158**, 116 (2016).
- [47] A. Griffith, *Philos. Trans. R. Soc. A-Math. Phys.* **221**, 163 (1921).
- [48] M. Wheeler, T. Wick, and W. Wollner, *Comput. Meth. Appl. Mech. Eng.* **271**, 69 (2014).
- [49] D. Santillán, R. Juanes, and L. Cueto-Felgueroso, *J. Geophys. Res.* **122**, 2565 (2017).
- [50] D. Santillán, J. Mosquera, and L. Cueto-Felgueroso, *Eng. Fract. Mech.* **178**, 109 (2017).
- [51] E. Detournay, *Int. J. Geomech.* **4**, 35 (2004).
- [52] J. I. Adachi and E. Detournay, *Eng. Fract. Mech.* **75**, 4666 (2008).
- [53] M. J. Hunsweck, Y. Shen, and A. J. Lew, *Int. J. Numer. Anal. Meth. Geomech.* **37**, 993 (2013).
- [54] B. Lecampion and E. Detournay, *Comput. Meth. Appl. Mech. Eng.* **196**, 4863 (2007).
- [55] E. Vanmarcke, *Random Fields: Analysis and Synthesis* (World Scientific, Singapore, 2010).
- [56] R. J. Hoeksema and P. K. Kitanidis, *Water Resour. Res.* **21**, 563 (1985).
- [57] P. Geyskens, A. Kiureghian, and P. Monteiro, *J. Struct. Eng.* **124**, 89 (1998).
- [58] T. Miranda, A. G. Correia, and L. R. e Sousa, *Int. J. Rock Mech. Min. Sci.* **46**, 1144 (2009).
- [59] M. Bolland, N. Desprat, D. Icard, S. Féréol, A. Asnacios, J. Browaeys, S. Hénon, and F. Gallet, *Phys. Rev. E* **74**, 021911 (2006).
- [60] S. Gui, R. Zhang, J. Turner, and X. Xue, *J. Geotech. Geoenviron. Eng.* **126**, 1 (2000).
- [61] H. Zhu, L. M. Zhang, L. Zhang, and C. Zhou, *Comput. Geotech.* **48**, 249 (2013).
- [62] A. A. Bakr, L. W. Gelhar, A. L. Gutjahr, and J. R. MacMillan, *Water Resour. Res.* **14**, 263 (1978).
- [63] A. L. Gutjahr, L. W. Gelhar, A. A. Bakr, and J. R. MacMillan, *Water Resour. Res.* **14**, 953 (1978).
- [64] L. W. Gelhar and C. L. Axness, *Water Resour. Res.* **19**, 161 (1983).
- [65] M. S. Cheung and W. Li, *Struct. Saf.* **25**, 245 (2003).
- [66] H. Duzgun, M. Yucemen, and C. Karpuz, *Rock Mech. Rock Eng.* **36**, 95 (2003).
- [67] R. Jimenez-Rodriguez, N. Sitar, and J. Chacon, *Int. J. Rock Mech. Min. Sci.* **43**, 847 (2006).
- [68] H. Zhu and L. M. Zhang, *Can. Geotech. J.* **50**, 723 (2013).
- [69] F. Ruan and D. McLaughlin, *Adv. Water Resour.* **21**, 385 (1998).
- [70] A. Gutjahr, B. Bullard, S. Hatch, and L. Hughson, *Stoch. Hydrol. Hydraul.* **8**, 79 (1994).
- [71] C. Miehe, M. Hofacker, and F. Welschinger, *Comput. Meth. Appl. Mech. Eng.* **199**, 2765 (2010).
- [72] C. Miehe, F. Welschinger, and M. Hofacker, *Int. J. Numer. Meth. Eng.* **83**, 1273 (2010).
- [73] C. Miehe, *Comput. Struct.* **66**, 37 (1998).
- [74] J. Vignollet, S. May, R. D. Borst, and C. Verhoosel, *Meccanica* **49**, 2587 (2014).
- [75] C. Kuhn, A. Schlüter, and R. Müller, *Comput. Mater. Sci.* **108**, 374 (2015).
- [76] A. Chambolle, *J. Math. Pures Appl.* **83**, 929 (2004).
- [77] S. Santucci, M. Grob, R. Toussaint, J. Schmittbuhl, A. Hansen, and K. Måløy, *Europhys. Lett.* **92**, 44001 (2010).
- [78] J. Hu and D. Garagash, *J. Eng. Mech.* **136**, 1152 (2010).
- [79] COMSOL MULTIPHYSICS, *Structural Mechanics Module User's Guide v5.2a* (Comsol, Stockholm, 2016).
- [80] A. C. Hindmarsh, P. N. Brown, K. E. Grant, S. L. Lee, R. Serban, D. E. Shumaker, and C. S. Woodward, *ACM Trans. Math. Softw.* **31**, 363 (2005).
- [81] C. Rosselló and M. Elices, *Cem. Concr. Res.* **34**, 1441 (2004).